THE RELATIONSHIP BETWEEN CAPILLARY PRESSURE, SATURATION AND INTERFACIAL AREA FROM A MODEL OF MIXED-WET TRIANGULAR TUBES

J.O. HELLAND[1] AND S.M. SKJÆVELAND[1]

[1]Department of Petroleum Engineering, Faculty of Science & Technology, University of Stavanger, N-4036 Stavanger

ABSTRACT

A simple bundle-of-triangular-tubes model is employed to calculate specific interfacial area for primary drainage, imbibition and secondary drainage for mixed-wet conditions. Accurate expressions for the capillary entry pressures are employed, that include the possibility of hinging interfaces in the corners due to contact angle hysteresis. Analytical expressions for specific interfacial area as a function of saturation and capillary pressure are derived for primary drainage, assuming that only the interfaces between bulk and corner fluid is contributive to interfacial area. Approximate correlations for interfacial area as a function of saturation are suggested for the subsequent imbibition and drainage processes. The correlations are fitted to the simulated data, and good agreement is obtained. We also demonstrate that hysteresis remains present in the relationship between interfacial area, capillary pressure and saturation when contact angle hysteresis is assumed. Hysteresis may be significant for both water-wet and mixed-wet conditions.

1. INTRODUCTION

Fluid-fluid interfacial area is recognized in the literature as an important parameter in understanding various multiphase flow processes in porous media. Mass transfer processes such as dissolution, adsorption and volatilization occur across interfaces and are strongly related to interfacial area. In particular, the coefficient for interfacial mass transfer rate is assumed to be proportional to the interfacial area [e.g., *Kennedy and Lennox*, 1997]. It has also been observed experimentally that surfactants and bacteria may preferentially accumulate at the fluid-fluid interfaces and affect the subsequent fluid transport [e.g., *Schäfer et al.*, 1998]. Thus the magnitude of the interfacial area is needed to quantify the efficiency and consequences of these processes.

Specific interfacial area between phase i and j is defined as

$$a_{ij} = \frac{1}{\mathcal{V}} \int_{\mathcal{S}_{ij}} d\mathcal{S}, \tag{1}$$

where $\mathcal{V}$ is a representative volume including both phases and $\mathcal{S}_{ij}$ is the total area of the interfaces in $\mathcal{V}$.

Despite the difficulties involved in direct measurements of the parameter a_{ij} as a function of saturation in porous media, progress has been made the last ten years to develop more reliable experimental methods. *Saripalli et al.* [1998]; *Schaefer et al.* [2000a] and *Faisal Anwar et al.* [2000] employed interfacial tracer techniques to determine the two-phase interfacial area using water-soluble surfactants. The mass of surfactant adsorbed at the interfaces was determined,

and the Gibbs adsorption equation was employed together with measurements of interfacial tensions to calculate the interfacial area. *Schaefer et al.* [2000b] used the same approach to determine three-phase interfacial area.

Pore-scale modelling represents an appealing approach to estimate the interfacial area explicitly and to study its functional dependencies. This is mainly due to the possibility of calculating several key parameters for multiphase flow simultaneously, which may be difficult or even impossible to obtain from experimental measurements. *Reeves and Celia* [1996] calculated the specific interfacial area between bulk fluids in a network constructed by conical pore throats of circular cross-sections. More recently, networks of angular pore shapes have been used to include the contribution of interfacial area from fluid-fluid interfaces in the corners of the pore space [*Dillard et al.*, 2001; *Dalla et al.*, 2002]. *Or and Tuller* [1999] and *Gladkikh and Bryant* [2003] have in addition included the area of thin films coating the pore walls in the calculations.

Other methods to calculate the interfacial area focus on the relationship between capillary pressure and saturation ($P_c - S$). Based on thermodynamics, *Bradford and Leij* [1997] estimated two- and three-phase interfacial area from measured $P_c - S$ data. *Oostrom et al.* [2001] derived analytical expressions for free and entrapped interfacial area as functions of water saturation by assuming the Brooks–Corey [*Brooks and Corey*, 1964] and the van Genuchten [*van Genuchten*, 1980] correlations for the $P_c - S$ relationship. The estimated expressions were in good agreement with experimental measurements.

Hassanizadeh and Gray [1993] argue that there exists a formal constitutive relationship between capillary pressure, saturation and specific interfacial area. They hypothesized that hysteresis in the $P_c - S$ relationship was an artifact of projecting the $P_c - S - a_{ij}$ surface onto the $P_c - S$ plane. New macroscale theories for multiphase flow have subsequently been developed that require the $P_c - S - a_{ij}$ relationship [e.g., *Gray*, 1999]. *Reeves and Celia* [1996] investigated the conjecture of *Hassanizadeh and Gray* [1993] with their network model. The a_{ij} surfaces plotted as a function of P_c and S displayed a characteristic convex shape which indicated that the functional relationship is nonunique, e.g., for any value of capillary pressure there corresponds at least two points on the surface with different saturations and the same specific interfacial area. *Held and Celia* [2001] calculated the a_{ij} surfaces with another network model, and the same convex shape was observed. They simulated imbibition and drainage scanning curves to cover the entire area within the bounding hysteretic $P_c - S$ loop and found a small separation between the imbibition and drainage surfaces. Thus they concluded that hysteresis was essentially eliminated in their numerical experiments. However, they only calculated interfacial area between the bulk fluids for water-wet conditions and hence neglected the impact mixed wettability and corner fluid occupancy have on the capillary pressure.

In this paper we use a physically-based bundle-of-triangular-tubes model to calculate two-phase specific interfacial area for mixed-wet conditions. The model is programmed in MATLAB[†] and has been shown to reproduce main features of two-phase capillary pressure curves for mixed-wet rock, scanning loops included [*Helland and Skjæveland*, 2004]. We derive analytical expressions for the specific interfacial area as a function of saturation and capillary pressure for primary drainage and propose approximate correlations for the specific interfacial area for subsequent imbibition and drainage processes. The correlations are compared with simulated

[†]MATLAB is a registered trademark of TheMathWorks Inc.

data. Finally, we challenge the conjecture of *Hassanizadeh and Gray* [1993] and explore if hysteresis can be eliminated for mixed-wet drainage and imbibition $P_c - S$ curves when specific interfacial area is incorporated in the relationship.

2. Model description

In this work we employ a pore-scale model with a bundle-of-tubes representation of the pore network, the tubes having equilateral, triangular cross-sections. This triangular geometry is readily described by the half angle of the corner, $\alpha = \pi/6$, and the inscribed radius R. The angular pore shape allows for representation of physical processes such as the establishment of mixed wettability within a single pore and drainage through fluid layers in the corners of the pore space [e.g., *Kovscek et al.*, 1993; *Hui and Blunt*, 2000]. In this section we review the aspects of the model which is relevant for the calculation of the specific interfacial area. The model is described in detail elsewhere [*Helland and Skjæveland*, 2004].

The cross-sectional fluid configurations that may occur in a tube for the sequence of processes primary drainage, imbibition, secondary drainage and secondary imbibition are shown in Figure 1. The curvatures across the interfaces in the corners are allowed to be positive or negative depending on the contact angles and the capillary pressure. Configuration A shows a tube that has always been waterfilled, while configuration B–G represent tubes that at some point have been invaded by oil. The bold lines indicate the lengths of the pore walls that have been contacted by oil and hence may have altered wettability after primary drainage. The distance b_{pd} from the apex of the corner to the position of the contact line at the end of primary drainage remains water-wet:

$$b_{pd} = \frac{\sigma \cos(\theta_{pd} + \alpha)}{P_c^{\max} \sin \alpha}, \tag{2}$$

where θ_{pd} is the contact angle, and $P_c^{\max}$ is the capillary pressure at the end of primary drainage.

Configuration B and C may occur for the first time during waterflooding when the water content in the corners has started to increase after primary drainage. Water invasion into configuration B is always a displacement to configuration D, while water invasion into configuration C is a displacement to configuration D or E. Configuration F may occur during secondary drainage when oil invades configuration E. Configuration G may occur for the first time during secondary imbibition when configuration B is invaded by water. Additionally, the oil layer displacements E to D and G to D may occur during imbibition, and the water layer displacement F to C and the oil layer displacement D to E may occur during drainage [*van Dijke and Sorbie*, 2006; *Helland and Skjæveland*, 2004]. To restrict the number of possible configurations we do not allow additional formation of interfaces in configuration F and G during subsequent saturation reversals. In theory, although not very likely, the number of interfaces in a cross-section could increase constantly as saturation reversals proceed, provided that contact angle hysteresis is large.

To account for contact angle hysteresis and wettability alteration we use a receding contact angle θ_{pd} in primary drainage, an advancing contact angle θ_a in imbibition, and a receding contact angle θ_r in secondary drainage. The contact angles satisfy $\theta_{pd} \leq \theta_r \leq \theta_a$.

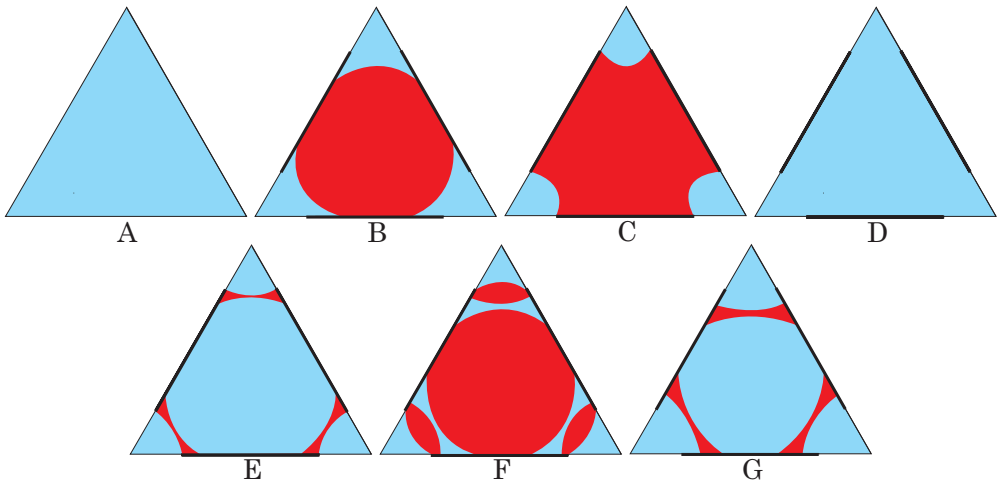

FIGURE 1. Fluid configurations for primary drainage, imbibition, secondary drainage, and secondary imbibition, with water in blue, and oil in red. The bold lines along the sides represent lengths of the pore walls where the wettability may have changed.

During piston-like displacements, new interfaces at positions $b > b_{pd}$ can only form in the corners if the contact angle satisfy the following condition:

$$\begin{aligned} \theta &< \frac{\pi}{2} - \alpha \quad \text{if bulk oil is bounded by water in the corner,} \\ \theta &> \frac{\pi}{2} + \alpha \quad \text{if bulk water is bounded by oil in the corner,} \end{aligned} \tag{3}$$

where θ is equal to θ_r, θ_{pd} or θ_a depending on the invasion process. However, if equation (3) is not satisfied, a new interface still forms at position $b = b_{pd}$ since then the interface is assumed to hinge with contact angle θ_h.

The capillary pressure across an interface in a corner is given by

$$P_c = \frac{\sigma}{r}, \tag{4}$$

where r is the radius of curvature measured through the oil phase.

To efficently handle configurations with more than one interface present in the corner, we introduce some notation. Interfaces are numbered in order from the corner towards the center of the cross-section. We apply the indicator notation

$$I^{(k)} = \begin{cases} 1 & \text{if interface } k \text{ bounds bulk oil and corner water,} \\ -1 & \text{if interface } k \text{ bounds bulk water and corner oil.} \end{cases} \tag{5}$$

Furthermore, the total number of interfaces present in a corner before displacement is denoted N^{init}, while the total number of interfaces after displacement is denoted N^{fin}. The cross-sectional *bulk* area bounded by interface k is denoted $A_b^{(k)}$. The bounding solid-fluid and oil-water lengths are denoted $L_s^{(k)}$ and $L_f^{(k)}$, respectively. These parameters are defined as follows:

$$A_b^{(k)} = \begin{cases} 3R^2 \cot\alpha - 3rb^{(k)} \sin(\beta^{(k)} + \alpha) + 3r^2\beta^{(k)} & \text{if } I^{(k)} = 1, \\ 3R^2 \cot\alpha - 3rb^{(k)} \sin(\beta^{(k)} - \alpha) - 3r^2\beta^{(k)} & \text{if } I^{(k)} = -1, \end{cases} \tag{6}$$

$$L_f^{(k)} = 6r\beta^{(k)}, \tag{7}$$

and

$$L_s^{(k)} = 6R \cot\alpha - 6b^{(k)}, \tag{8}$$

where

$$b^{(k)} \sin\alpha = r \sin\beta^{(k)}, \tag{9}$$

and

$$\beta^{(k)}(\theta^{(k)}) = \begin{cases} \dfrac{\pi}{2} - \alpha - \theta^{(k)} & \text{if } I^{(k)} = 1, \\ \dfrac{\pi}{2} + \alpha - \theta^{(k)} & \text{if } I^{(k)} = -1. \end{cases} \tag{10}$$

Equations (6)–(10) are written with general contact angles $\theta^{(k)}$ that may be equal to $\theta_h^{(k)}$, θ_r or θ_a. Notice also that $b^{(1)} = b_{pd}$ in configuration C, E and F.

After a reversal of saturation change, the interfaces in the corners, if present, may be stuck at fixed positions while the contact angle changes with capillary pressure. Using equations (4), (9) and (10), interface k hinges according to

$$\theta_h^{(k)} = \begin{cases} \arccos\left(\dfrac{P_c b^{(k)} \sin\alpha}{\sigma}\right) - \alpha & \text{if } I^{(k)} = 1, \\ \arccos\left(\dfrac{P_c b^{(k)} \sin\alpha}{\sigma}\right) + \alpha & \text{if } I^{(k)} = -1. \end{cases} \tag{11}$$

If the advancing or receding contact angle is reached prior to piston-like invasion, the interfaces in the corners begin to move at constant contact angles during a further change of capillary pressure. The position $b^{(k)}$ of interface k is then changing according to

$$b^{(k)} = \begin{cases} \dfrac{\sigma}{P_c} \dfrac{\cos(\theta^{(k)} + \alpha)}{\sin\alpha} & \text{if } I^{(k)} = 1, \\ \dfrac{\sigma}{P_c} \dfrac{\cos(\theta^{(k)} - \alpha)}{\sin\alpha} & \text{if } I^{(k)} = -1. \end{cases} \tag{12}$$

where $\theta^{(k)}$ is equal to θ_{pd} in primary drainage, θ_a in imbibition, and θ_r in secondary drainage.

2.1. **Capillary entry pressures.** The capillary entry pressures for piston-like invasion are calculated from an energy balance equation which equates the virtual work with the associated change in surface free energy for a small displacement of the invading interface in the direction along the tube length. The energy balance equation relates the effective entry radius of curvature, expressed by r, to the cross-sectional area exposed to change of fluid occupancy, the bounding cross-sectional fluid-solid and fluid-fluid lengths, and the contact angle θ [e.g., *Ma*

et al., 1996; *Øren et al.*, 1998]. To account for all the allowed displacements between configurations A–G (both bulk and layer displacements), the energy balance may be formulated as follows using the notation from equations (4)–(10):

$$\begin{aligned}&\frac{1}{r}(\textstyle\sum_{k=1}^{N^{\text{fin}}} A_b^{(k)} I^{(k)} - \sum_{k=1}^{N^{\text{init}}} A_b^{(k)} I^{(k)}) = \\ &\cos\theta(\textstyle\sum_{k=1}^{N^{\text{fin}}} L_s^{(k)} I^{(k)} - \sum_{k=1}^{N^{\text{init}}} L_s^{(k)} I^{(k)}) + (\sum_{k=1}^{N^{\text{fin}}} L_f^{(k)} - \sum_{k=1}^{N^{\text{init}}} L_f^{(k)}).\end{aligned} \tag{13}$$

where θ is equal to θ_{pd}, θ_a and θ_r for primary drainage, imbibition and secondary drainage, respectively.

If invasion occurs while the interfaces in the corners hinge at fixed positions $b^{(k)}$, then $\theta^{(k)} \neq \theta$, and equation (13) is solved iteratively together with equations (6)–(9) to obtain a converged value of r. When $\theta^{(k)} = \theta$, explicit expressions for r are derived by combining equations (6)–(10) and (13). This is always the case in primary drainage, i.e., $\theta^{(1)} = \theta = \theta_{pd}$. The capillary entry pressure is finally calculated from equation (4).

3. Calculation of interfacial area

Since we assume a model of straight triangular tubes, it suffices to consider the cross-sections when calculating saturation and specific interfacial area. The cross-sectional area A of a tube is related to the radius of the inscribed circle, R, by

$$A = 3R^2 \cot\alpha. \tag{14}$$

To calculate the area of oil and water occupied in corners and layers we use combinations of the following equation with appropriate arguments ψ:

$$A_c(\psi) = 3r^2(\psi + \alpha - \frac{\pi}{2} + \cos\psi(\frac{\cos\psi}{\tan\alpha} - \sin\psi)). \tag{15}$$

As an example, the area of water in the corners of configuration C is given by $A_c(\theta_h^{(1)})$, whereas the area of oil in layers of configuration E is calculated from $A_c(\pi - \theta_a) - A_c(\theta_h^{(1)})$ when the interfaces bounding bulk water are advancing towards the corners. Thus, equation (14) and (15) constitute the expressions required to calculate the saturation.

Specific interfacial area is calculated from equation (1) by adding the lengths of all oil-water interfaces in the corners of the tubes and dividing by the total cross-sectional tube area in the bundle. The interfacial lengths are readily expressed in terms of equation (7) with the appropriate values for $\beta^{(k)}$ and $\theta^{(k)}$:

$$L_f^{(k)} = 6r\beta^{(k)}(\theta^{(k)}). \tag{16}$$

As an example, the interfacial length in configuration C with hinging interfaces is $6r\beta^{(1)}(\theta_h^{(1)})$. The interfacial length in configuration E is given by $6r\beta^{(1)}(\theta_h^{(1)}) + 6r\beta^{(2)}(\theta_a)$ if the interfaces surrounding bulk water advance towards the corners. Since the model only accounts for cross-sectional configurations, it is not possible to calculate interfacial area between bulk phases. Moreover, we neglect the contribution to interfacial area from possible thin films along the sides of the tubes.

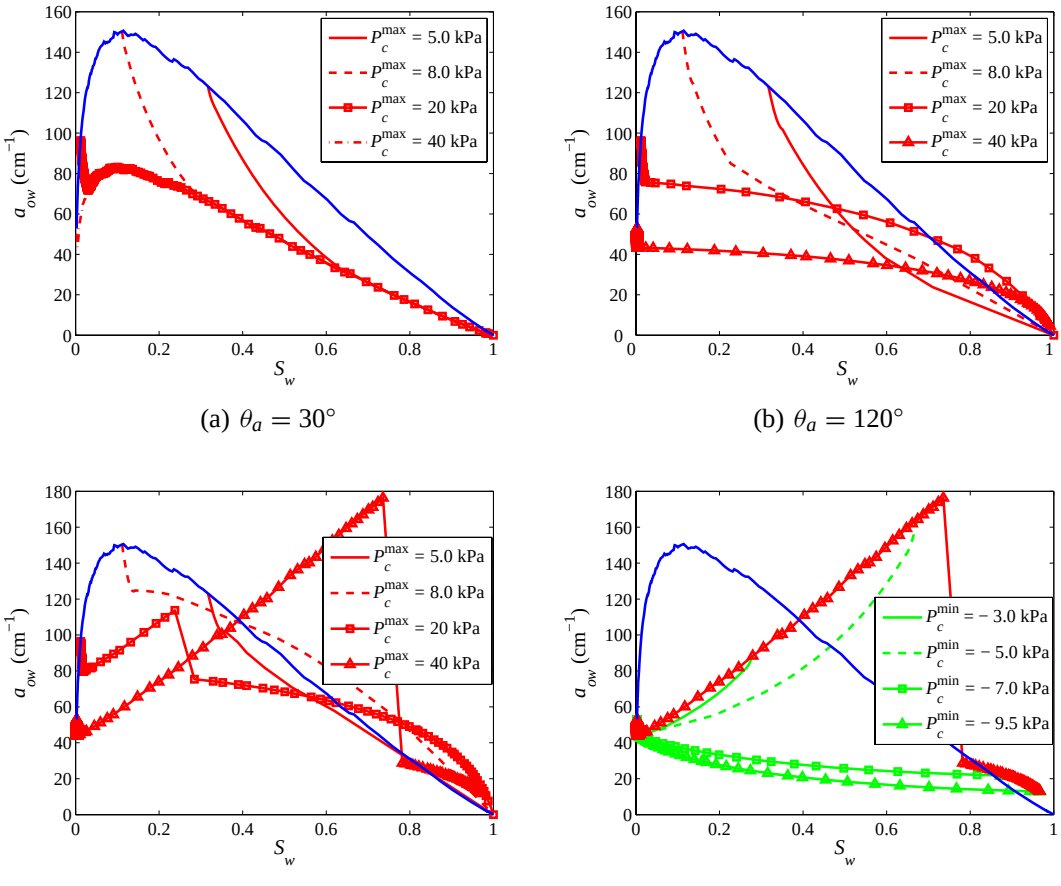

(a) $\theta_a = 30°$ (b) $\theta_a = 120°$

(c) $\theta_a = 180°$ (d) $\theta_a = 180°, \theta_r = 70°$

FIGURE 2. Specific interfacial area vs. saturation plotted for primary drainage (in blue), imbibition (in red) and secondary drainage (in green). (a)–(c) Effect of reversal point and advancing contact angle on imbibition. (d) Effect of reversal point on secondary drainage.

3.1. **Numerical examples.** We have performed simulations of the specific interfacial area vs. saturation relationship for primary drainage, imbibition and secondary drainage. For this purpose we assume that the pore-size density is described by a truncated Weibull distribution [*Dong et al.*, 1995; *Hui and Blunt*, 2000]. The pore sizes R are generated in the following manner: Pick random numbers $x \in [0, 1]$ and calculate inscribed radii from

$$R = R_{\text{ch}}\Big(- \ln[(1-x)\exp(-\Big[\frac{R_{\max} - R_{\min}}{R_{\text{ch}}}\Big]^{\eta}) + x]\Big)^{\frac{1}{\eta}} + R_{\min}, \tag{17}$$

where $R_{\min}$, $R_{\min}$ and R_{ch} are the inscribed radii of the largest, smallest and characteristic pore sizes, respectively, and η is a dimensionless parameter. In the simulations we set $R_{\min} = 0\mu$m, $R_{\max} = 100\mu$m, $R_{\text{ch}} = 15\mu$m and $\eta = 1.5$. Furthermore, $\sigma = 0.050$ N/m and $\theta_{pd} = 0°$.

Figure 2(a)–(c) show imbibition interfacial area curves initiated from different saturation reversal points after primary drainage for three different advancing contact angles. The $a_{ow}(S_w)$ curves for primary drainage exhibit the same general trends as measured data [*Faisal Anwar*

et al., 2000; *Schaefer et al.*, 2000b; *Oostrom et al.*, 2001]. However, the shape of the imbibition curve is very sensitive to the reversal point. When $\theta_a = 30°$, piston-like invasion may either occur by displacements from configuration C to D, or from B to D. The first displacement occurs for small $P_c^{\max}$ when the amount of water in the corner is large. For large $P_c^{\max}$, the interfaces in the corners move towards the center of the pore, and configuration B forms. The fraction of water area in the corners is larger in the small pores since the distance b_{pd} does not depend on pore size. Thus, configuration B may only form in the larger pores. The entry pressure for the direct displacement from configuration C to D depends on b_{pd}, and thereby $P_c^{\max}$. This sensitivity is visible in the interfacial area curves starting at $P_c^{\max} = 5.0$ kPa and $P_c^{\max} = 8.0$ kPa where the displacement C to D occurs first. Subsequently, the displacement B to D occurs along the segments of the curves that coincide for different the $P_c^{\max}$ values. The imbibition curves originating from larger $P_c^{\max}$ exhibit a steep decrease of interfacial area until a local minimum is reached. This decrease of a_{ow} is caused by the displacement from configuration C to D, which still occurs in a few of the smaller pores initially, and by the interfaces in the corners of configuration C that hinge as P_c decreases. When $\theta_h^{(1)} = \theta_a$, the interfaces start to move towards the center of the pore with a constant contact angle θ_a, and configuration B forms. This latter displacement results in an increased a_{ow}.

Figure 2(b) demonstrates the effect of reversal point on imbibition interfacial area when $\theta_a = 120°$. In this case, piston-like invasion always occurs by displacements from configuration C to D. In the initial stage, a_{ow} decreases steeply due to the hinging interfaces in configuration C. The displacement to configuration D is very sensitive to $P_c^{\max}$ when $\theta_a > 90°$, and invasion of the pore sizes may not necessarily occur in monotonically decreasing order. *Helland and Skjæveland* [2004] pointed out that the fraction of water-wet pore-wall surface is larger in the smaller pores than in the larger ones since the distance b_{pd} does not depend on pore size. Thus, the water in the corners, separated by hinging interfaces, affects the entry pressures increasingly as pore size decreases. For small $P_c^{\max}$, water preferentially invades the smaller pores first, which results in a pronounced decrease of interfacial area as water saturation increases. For larger $P_c^{\max}$, water preferentially invades the larger pore sizes first. As shown in Figure 2(b), this results in a less pronounced decrease of interfacial area. For intermediate $P_c^{\max}$, water may start to invade the larger and smaller pore sizes simultaneously [*Helland and Skjæveland*, 2004].

Figure 2(c) shows the results for $\theta_a = 180°$. The imbibition processes starting from $P_c^{\max} = 5.0$ kPa and $P_c^{\max} = 8.0$ kPa occur by displacements from configuration C to D. Thus, the interfacial area curves display similar trends as observed in Figure 2(b). However, for $P_c^{\max} = 20$ kPa and $P_c^{\max} = 40$ kPa, the displacement from configuration C to E occurs in the larger pores, leading to a significant increase of a_{ow}. The interfacial area decreases abruptly when the layer displacement from configuration E to D occurs. Subsequently, the imbibition proceeds with displacements from configuration C to D, which results in a less pronounced decrease of a_{ow}.

Figure 2(d) shows secondary drainage curves initiated from different reversal points on the imbibition curve in Figure 2(c) with $P_c^{\max} = 40$ kPa. The capillary pressures at the reversal points are denoted $P_c^{\min}$. In this example the displacement from configuration E to C occurs for large values of $P_c^{\min}$. Because of the large contact angle hysteresis assumed ($\theta_a = 180°$ and $\theta_r = 70°$), this displacement occurs while the interfaces separating bulk water from oil in layers hinge. *Helland and Skjæveland* [2004] demonstrated that the invasion order of the pore sizes for this displacement is sensitive to $P_c^{\min}$ when $\theta_r < 90°$, and that the presence of oil layers tend

to decrease the entry pressure. This is opposed to the behaviour of the displacement between configuration D and C, where the presence of water in the corners tends to increase the entry pressure. In Figure 2(d), the displacement E to C occurs preferentially in the order of increasing pore size, and hence the decrease of a_{ow} is most conspicuous at the initial stages of the drainage curves. For the small $P_c^{\min}$ values, where configuration E has ceased to exist, invasion occur in the order of decreasing pore size, and the increase of interfacial area is most pronounced at the final stages of the drainage curves. Obviously, if a sufficiently small receding contact angle is considered, the displacement D to B will occur instead, implying that these drainage curves will resemble the general trends of the primary drainage curve. On the other hand, if θ_r is close to θ_a, the *layer* displacement D to E may occur instead, implying that the drainage curves will reproduce the shape of the complex imbibition curve.

3.2. **Analytical correlations for primary drainage.** To develop analytical expressions for specific interfacial area in primary drainage, we assume the simple pore-size density

$$f(R) = \nu R_{\max}^{-\nu} R^{\nu-1}, \tag{18}$$

which includes the adjustable parameter $\nu > 0$. The uniform case corresponds to $\nu = 1$. *Helland and Skjæveland* [2004] have shown that this pore-size density is compatible with the Brooks-Corey correlation if no water is residing in the corners after oil invasion, or if a bundle-of-cylindrical-tubes model is assumed. The water saturation was expressed as a sum of two terms,

$$S_w = S_{wb} + S_{wc}, \tag{19}$$

where S_{wb} is the contribution from the tubes completely filled with water, and S_{wc} is the contribution from the tubes with water residing in the corners after invasion. It was found that

$$S_{wb} = \Big(\frac{c}{P_c}\Big)^{\nu+2}, \tag{20}$$

and

$$S_{wc} = \epsilon \frac{\nu+2}{\nu}\Big(\frac{c}{P_c}\Big)^2\Big[1 - \Big(\frac{c}{P_c}\Big)^{\nu}\Big], \tag{21}$$

where ϵ is a geometry factor given by

$$\epsilon = \frac{g_1}{g_2}, \tag{22}$$

with

$$g_1(\theta_{pd}) = \cos\theta_{pd} - \sqrt{\frac{\tan\alpha}{2}(\sin 2\theta_{pd} - 2\theta_{pd} - 2\alpha + \pi)}, \tag{23}$$

and

$$g_2(\theta_{pd}) = \cos\theta_{pd} + \sqrt{\frac{\tan\alpha}{2}(\sin 2\theta_{pd} - 2\theta_{pd} - 2\alpha + \pi)}. \tag{24}$$

The capillary entry pressure c for the largest pore size $R_{\max}$ is found by combining equation (6)–(10) with $\theta^{(1)} = \theta = \theta_{pd}$. This results in the relation

$$c = \frac{\sigma}{R_{\max}} g_2. \tag{25}$$

By equation (20), capillary pressure may be expressed in terms of the bulk saturation as

$$P_c = c S_{wb}^{-a}, \tag{26}$$

where the pore-size distribution index a is related to ν by

$$a = \frac{1}{\nu + 2}. \tag{27}$$

If $S_{wc} = 0$, which corresponds to the case when no water is residing in the corners after oil invasion, the Brooks-Corey correlation [*Brooks and Corey*, 1964],

$$P_c = cS_w^{-a}, \tag{28}$$

is valid.

To derive analytical expressions for the specific interfacial area, we employ the definition given by equation (1) as a starting point. For the bundle of triangular tubes, equation (1) yields

$$a_{ow} = \frac{L_f^{(1)} \int_{R_o}^{R_{\max}} f\, dR}{\int_0^{R_{\max}} f A\, dR}, \tag{29}$$

since the length $L_f^{(1)}$ is independent of pore size. The pore size invaded by oil at capillary pressure P_c is denoted R_o. By combining equation (6)–(10), we find that P_c is related to R_o by

$$R_o = \frac{\sigma}{P_c} g_2. \tag{30}$$

Furthermore, with $L_f^{(1)} = 6r\beta^{(1)}(\theta_{pd})$ and $r = \sigma / P_c$, equation (29) may be written as

$$a_{ow} = \frac{2c\beta^{(1)} \tan\alpha}{\sigma g_2^2} \frac{\nu + 2}{\nu} \frac{c}{P_c} \Big[1 - \Big(\frac{c}{P_c} \Big)^{\nu} \Big]. \tag{31}$$

Equation (31) relates specific interfacial area to capillary pressure. Equation (26) may be inserted into equation (31) to provide an equation which relates specific interfacial area to bulk water saturation:

$$a_{ow} = \frac{2c\beta^{(1)} \tan\alpha}{\sigma g_2^2} \frac{\nu + 2}{\nu} S_{wb}^{\frac{1}{\nu+2}} \Big[1 - S_{wb}^{\frac{\nu}{\nu+2}} \Big]. \tag{32}$$

Moreover, a comparison between equations (21), (31) shows that corner water saturation is related to specific interfacial area by

$$a_{ow} = \frac{2P_c\beta^{(1)} \tan\alpha}{g_1 g_2 \sigma} S_{wc}. \tag{33}$$

We have solved equations (19)–(21) and calculated specific interfacial area from equation (31) for different combinations of $R_{\max}$ and ν. The results are presented in Figure 3. The level of specific interfacial area and capillary pressure is more sensitive to variations of $R_{\max}$ than to variations of ν. The level of interfacial area is increased if the range of pore sizes is reduced. The $a_{ow}(S_w)$ curves exhibit the same general trends as measured primary drainage data [*Faisal Anwar et al.*, 2000; *Schaefer et al.*, 2000b; *Oostrom et al.*, 2001].

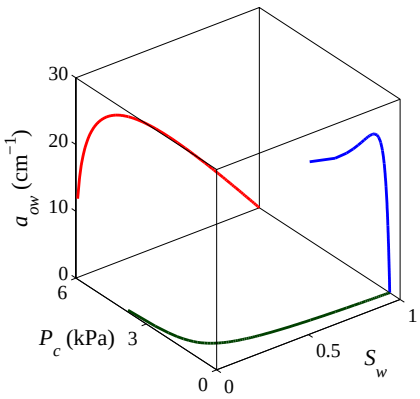

(a) $\nu = 0.5$, $R_{\max} = 200\mu$m

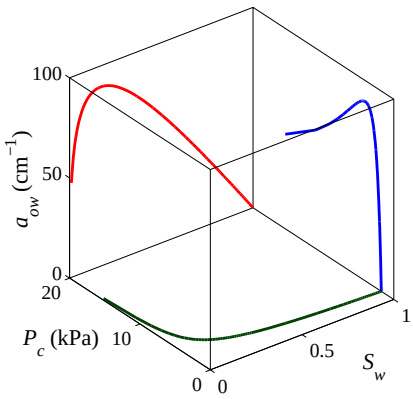

(b) $\nu = 0.5$, $R_{\max} = 50\mu$m

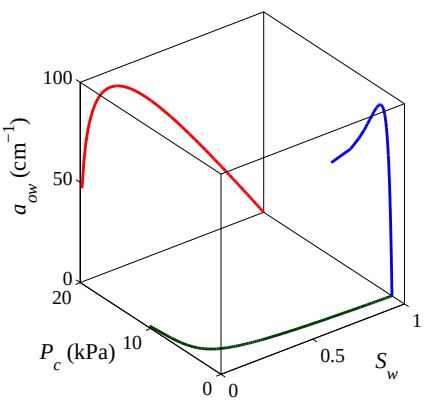

(c) $\nu = 1.5$, $R_{\max} = 50\mu$m

FIGURE 3. Primary drainage $a_{ow}(S_w)$, $a_{ow}(P_c)$ and $P_c(S_w)$ curves calculated from equations (19)–(21) and (31) using three different combinations of ν and $R_{\max}$.

3.3. **Approximate correlations for the bounding hysteresis loop.** Since the bulk water saturation is much larger than the corner water saturation in most of the saturation range, we propose to formulate interfacial area as a function of total water saturation by employing the same functional form as in equation (32). Different rock and fluid properties are accounted for by including adjustable parameters. Thus, for water-wet media we propose the correlation

$$a_{ow} = u_w S_w^{v_w}(1 - S_w^{q_w}), \tag{34}$$

where the three parameters u_w, v_w and q_w have to be determined. Obviously, u_w has the same dimension as specific interfacial area, whereas v_w and q_w are dimensionless.

For water invasion into a complete oilfilled and oil-wet bundle of triangular tubes with equation (3) satisfied for θ_a, an expression similar to equation (32) can be derived where the bulk water saturation is replaced by the bulk oil saturation. For mixed-wet conditions we propose to formulate the interfacial area as a sum of two terms where one term is expressed by the water

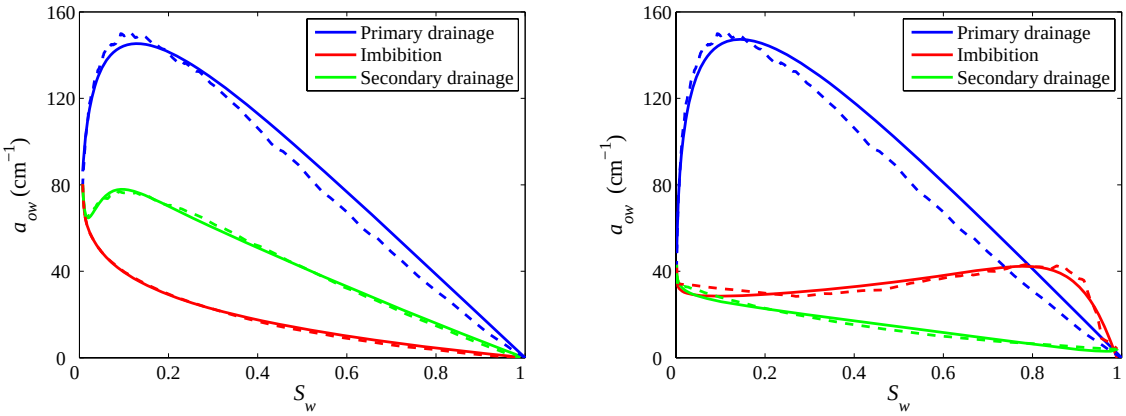

(a) Water-wet case (b) Mixed-wet case

FIGURE 4. Specific interfacial area plotted against water saturation for primary drainage, imbibition and secondary drainage. Simulation results are shown by broken lines, while the proposed correlations fitted to the simulated data are represented by the solid lines.

saturation, as in equation (34), while the other term is expressed by the oil saturation. This results in the correlation

$$a_{ow} = u_w S_w^{v_w}(1 - S_w^{q_w}) + u_o S_o^{v_o}(1 - S_o^{q_o}), \tag{35}$$

where the two sets of the parameters u, v, q have to be determined. The oil saturation term is intended to dominate at small oil saturations, while the water saturation term should dominate at small water saturations. For mixed-wet conditions, interfacial area may decrease at small water saturations in imbibition because of the displacement from configuration C to D. The interfacial area may start to increase at larger water saturations due to the formation of oil layers in the displacement from configuration C to E. When the oil layers are displaced, interfacial area decreases abruptly. Equation (35) accounts for such behaviour since the proposed correlation may yield a local minimum and a local maximum of interfacial area.

To investigate the flexibility of equation (34) and (35), we have fitted the correlations to simulated data. For this purpose we consider the Weibull distributed pore sizes which were employed to simulate the $a_{ow}(S_w)$ curves in Figure 2. We still assume $\sigma = 0.050$ N/m and $\theta_{pd} = 0°$ during primary drainage. In the subsequent imbibition and drainage processes, we consider randomly distributed contact angles. For water-wet conditions we assume $\theta_a \in [50°, 80°]$, while for mixed-wet conditions we assume $\theta_a \in [90°, 180°]$. The receding contact angles are calculated by $\theta_r = 0.5\theta_a$ for both water-wet and mixed-wet conditions. The primary drainage curve for the water-wet system is terminated at $P_c^{\max} = 25$ kPa, and for the mixed-wet system, primary drainage is terminated at $P_c^{\max} = 50$ kPa to facilitate for oil layer formation in the subsequent invasion processes.

Equation (34) is fitted to the primary drainage curve, while equation (35) is fitted to the main imbibition and secondary drainage curves. A standard curvefitting method is employed to determine the correlation parameters. The results are shown in Figure 4, and the correlations agree fairly well with the simulated data. A better match may be obtained using appropriate error

weighting. A comparison between equations (34), (35) and (32) indicates that all parameters are likely to be positive. However, to obtain a good match beetween the correlations and the simulated data, one or two of the parameters in equation (35) turns out to be slightly negative in some cases.

There is a paucity of measured imbibition and secondary drainage interfacial area data in the literature. However, the imbibition curve in Figure 4(b) seems to display similar trends as imbibition measurements [Figure 5, *Schaefer et al.*, 2000a]. Nevertheless, more data is required to validate the correlations and to determine the applicability of the model to predict general trends in interfacial area for various conditions.

4. THE CONJECTURE OF *Hassanizadeh and Gray* [1993]

To investigate if hysteresis is absent in the $P_c - S_w - a_{ow}$ relationship, as proposed by *Hassanizadeh and Gray* [1993], we employ our simple bundle-of-tubes model to perform the same exercise as *Held and Celia* [2001]. They utilized a network model and generated a drainage a_{ow} surface from drainage scanning curves initiated from different reversal points on the main imbibition curve. Similarly, an imbibition a_{ow} surface was generated by imbibition scanning curves initiated from different reversal points on the main secondary drainage curve. If the intersections of the two surfaces at constant P_c follow the same $a_{ow}(S_w)$ curve, then hysteresis is absent. *Held and Celia* [2001] found that the intersections essentially followed the same $a_{ow}(S_w)$ curve, and hence they concluded that the conjecture of *Hassanizadeh and Gray* [1993] could not be rejected. However, *Held and Celia* [2001] only considered water-wet media and neglected the contribution of interfacial area from interfaces present in corners of the pore space.

We explore if hysteresis can be eliminated when only interfaces between bulk and corner fluids is contributive to interfacial area. The water-wet and mixed-wet cases modelled in Section 3.3 are both examined. After primary drainage, configuration A remains in a few of the smaller tubes. Imbibition is terminated when $S_w = 1$ in the water-wet case. In the mixed-wet case, imbibition is terminated when $S_w = 0.99$. At this stage, configuration E has ceased to exist.

The drainage and imbibition a_{ow} surfaces for the water-wet case are shown in Figure 5(a), (b), respectively, with the bounding hysteresis loop marked by bold lines. The surfaces display a concave-convex shape with scanning curves that may exhibit local minima and local maxima. This clearly deviates from the results by *Reeves and Celia* [1996]; *Held and Celia* [2001] who found that the surfaces were convex in both the $S_w - a_{ow}$ and the $P_c - a_{ow}$ plane. The only resemblance is the local convex shape of the drainage surface in the $S_w - a_{ow}$ plane, implying that for any value of capillary pressure there exists at least two points on the surface with different saturations and equal interfacial area. The projections onto the $a_{ow} - S_w$ plane show that the drainage $a_{ow}(S_w)$ scanning curves have a convex shape with a local maximum of a_{ow} at an intermediate value of S_w, and a local minimum at a very small water saturation, which is similar to the secondary drainage curve in Figure. 4(a). The imbibition surface in Figure 5(b) are constructed by scanning curves that decreases monotonically with increasing water saturation. This clearly deviates from the results of *Reeves and Celia* [1996]; *Held and Celia* [2001]. The sharp decrease of the imbibition a_{ow} surface is caused by the significant contact angle hysteresis assumed in our simulations, which causes the interfaces to hinge instead of moving with constant contact angles towards the center of the cross-sections prior to piston-like water invasion.

Intersections of the drainage and imbibition a_{ow} surfaces for three constant values of P_c are shown in Figure 5(c). Evidently, very different values of specific interfacial area occurs for

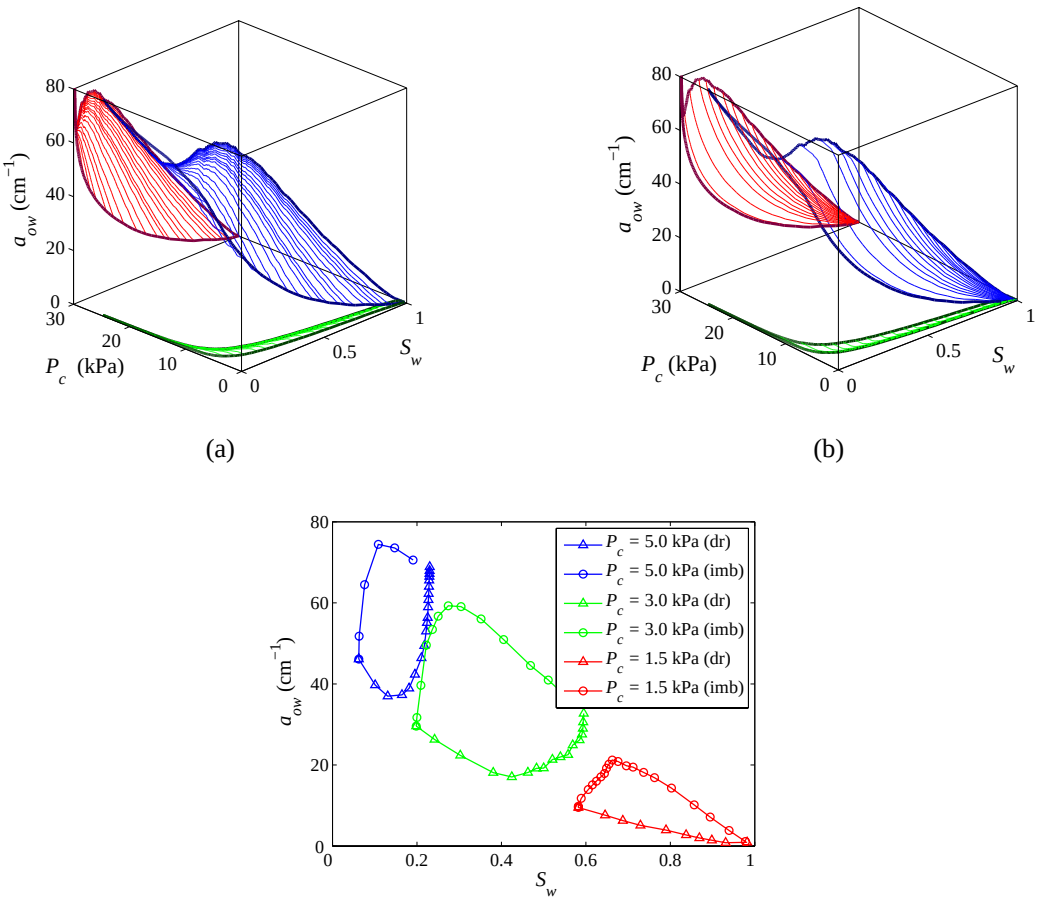

FIGURE 5. Specific interfacial area a_{ow} plotted as a function of P_c and S_w for water-wet conditions. Projections onto the $P_c - S_w$ plane (green) and $a_{ow} - S_w$ plane (red) are also shown. The bounding hysteresis loop is marked by the bold lines. (a) Surface created by drainage scanning curves. (b) Surface created by imbibition scanning curves. (c) Planes at three constant P_c through the drainage (dr) and imbibition (imb) a_{ow} surfaces.

the different directions of saturation change, implying that hysteresis remains present in the $P_c - S_w - a_{ow}$ relationship. Notice also that the imbibition interfacial area is higher than the drainage interfacial area for a constant value of capillary pressure. It should be emphasized that this does not imply that interfacial area is higher in imbibition than in drainage for a specific scanning loop. This feature is explained as follows: imbibition scanning curves are initiated from the main secondary drainage curve where interfacial area may be large, while drainage scanning curves are initiated from the main imbibition curve where interfacial area may be small. Because of the significant contact angle hysteresis assumed, the different scanning curves may reach the chosen level of constant capillary pressure before piston-like invasion results in pronounced changes of interfacial area. The differences between drainage and imbibition

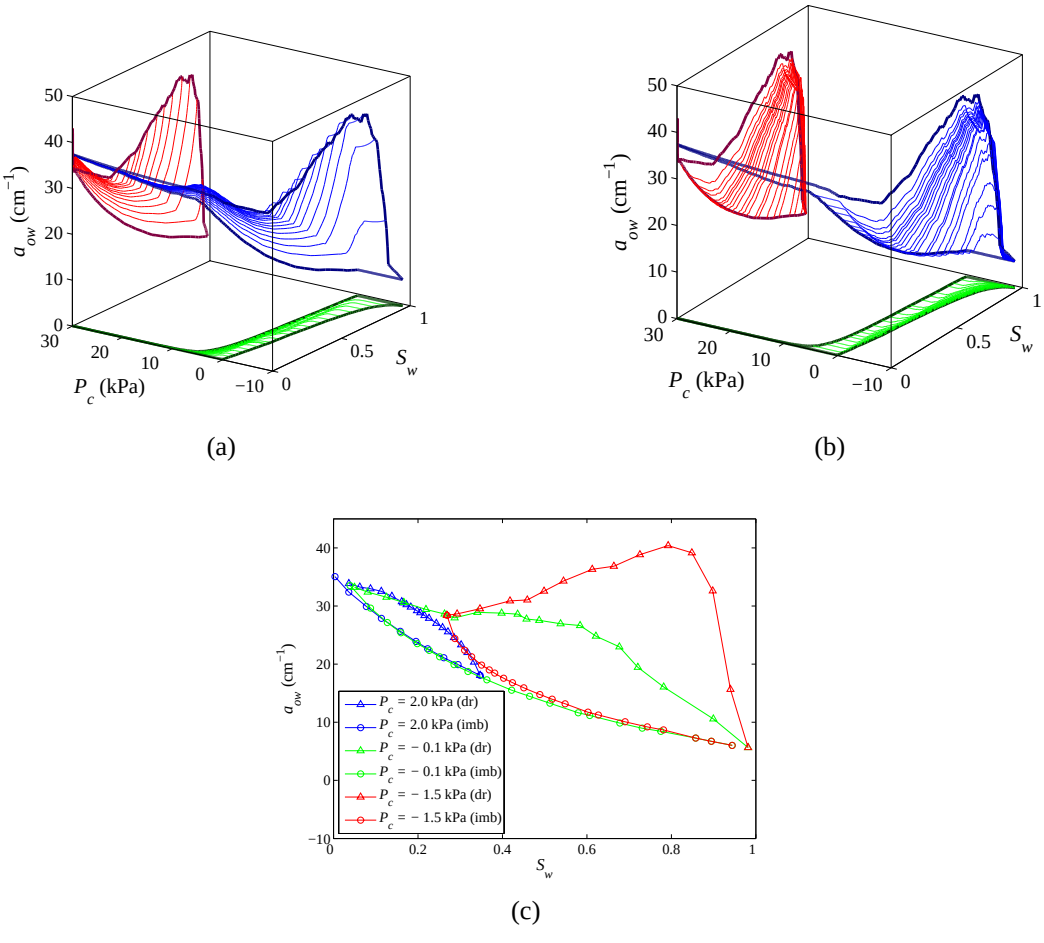

FIGURE 6. Specific interfacial area a_{ow} plotted as a function of P_c and S_w for mixed-wet conditions. Projections onto the $P_c - S_w$ plane (green) and $a_{ow} - S_w$ plane (red) are also shown. The bounding hysteresis loop is marked by the bold lines. (a) Surface created by drainage scanning curves. (b) Surface created by imbibition scanning curves. (c) Planes at three constant P_c through the drainage (dr) and imbibition (imb) a_{ow} surfaces.

interfacial area decreases as water saturation increases. This is due to the shape of the projection of the bounding hysteresis loop in the $a_{ow} - S_w$ plane shown in Figure 5(a), (b).

The corresponding results for the mixed-wet case are presented in Figure 6. The projections onto the $a_{ow} - S_w$ plane reveal that the interfacial area is higher during main imbibition than during main secondary drainage, as opposed to the results for water-wet conditions. The a_{ow} surfaces display a more complex shape for the mixed-wet case because of oil layer formation during imbibition. After primary drainage, the interfaces are hinging until the displacements from configuration C to D occur, resulting in a decrease of interfacial area at small water saturations in imbibition. For larger water saturations, the displacements from configuration C to E occur, resulting in an increased interfacial area. When the interfaces that separate oil layers from bulk water move towards the corners, the interfacial area starts to decrease slightly. Eventually,

the oil layers are displaced and the interfacial area decreases abruptly. These trends are also present in the imbibition scanning curves, as they display a concave-convex shape with a local minimum and a local maximum. This is demonstrated in Figure 6(b). In the drainage processes, the displacement from configuration E to C dominates at intermediate/large water saturations, while the displacement from configuration D to C dominates at small water saturations. Thus, the drainage scanning curves display concave shapes in the $a_{ow} - S_w$ plane, as shown in Figure 6(a). Following the same reasoning as for the water-wet case, it is expected that the $a_{ow}(S_w)$ curves produced by intersections of the surfaces at constant P_c, result in higher interfacial area in drainage than in imbibition, as shown in Figure 6(c). Moreover, the differences between drainage and imbibition interfacial area increases according to the water saturation. This is due to the shape of the projection of the bounding hysteresis loop in the $a_{ow} - S_w$ plane shown in Figure 6(a), (b). Evidently, Figure 6(c) indicates that hysteresis in the $P_c - S_w - a_{ow}$ relationship remains present for mixed-wet conditions as well.

5. Summary and conclusions

We have used a simple bundle-of-triangular-tubes model to calculate interfacial area as a function of saturation for primary drainage, imbibition and secondary drainage for mixed-wet conditions. The model employs accurate expressions for the capillary entry pressures, accounting for the possibility of hinging interfaces in the corners due to contact angle hysteresis. Analytical expressions for specific interfacial area as a function of saturation and capillary pressure are derived for primary drainage, assuming that only the interfaces between bulk and corner fluid is contributive to interfacial area. Flexible correlations are suggested for the subsequent imbibition and secondary drainage processes. We have also investigated if hysteresis occurs in the relationship between capillary pressure, saturation and interfacial area. The specific conclusions are as follows:

(i) The analytically derived correlations imply that the capillary pressure vs. saturation relationship and the interfacial area vs. saturation relationship are equivalent in primary drainage of triangular tubes.

(ii) The proposed correlations are in agreement with the interfacial area data generated by the model. Experimental measurements of hysteresis loops are required to validate the correlations and to determine the applicability of the model for interfacial area calculations.

(iii) Hysteresis in the relationship between capillary pressure, saturation and corner fluid – bulk fluid interfacial area remains present between imbibition and secondary drainage processes if contact angle hysteresis is assumed. Hysteresis may be significant for both water-wet and mixed-wet conditions.

Nomenclature

A	Cross-sectional area
a	Specific interfacial area
b	Position of arc meniscus
f	Pore-size density
g_1	Geometry factor, see equation (23)
g_2	Geometry factor, see equation (24)

I	Indicator notation, see equation (5)
L_s	Cross-sectional fluid-solid length
L_f	Cross-sectional fluid-fluid length
N	Total number of AMs present in a corner
P	Pressure
q	Correlation parameter, see equations (34), (35)
r	Radius of curvature
R	Radius of the inscribed circle
S	Saturation
$\mathcal{S}$	Total area of interfaces within a representative volume
u	Correlation parameter, see equations (34), (35)
$\mathcal{V}$	Representative volume
v	Correlation parameter, see equations (34), (35)
x	Random number between 0 and 1
α	Corner half angle
β	Angle defined from geometry of the interfaces in the corners, see equation (10)
ϵ	Geometry factor, see equation (22)
η	Parameter in the Weibull distribution
θ	Contact angle
ν	Parameter in pore-size distribution
σ	Interfacial tension
ψ	Angle

Subscripts.

a	Advancing
b	Bulk
c	Corner or capillary
ch	Characteristic
h	Hinging
max	Maximum
min	Minimum
o	Oil
pd	Primary drainage
r	Receding
w	Water

Superscripts.

fin	Final
init	Initial
(k)	AM number counted in order from corner towards center
max	Maximum
min	Minimum

ACKNOWLEDGEMENTS

Support for Johan Olav Helland was provided by Statoil through the VISTA program.

REFERENCES

Bradford, S. A., and F. J. Leij (1997), Estimating interfacial areas for multi-fluid soil systems, *J. Cont. Hydr.*, *27*, 83–105.

Brooks, R. H., and A. T. Corey (1964), Hydraulic properties of porous media, hydraulic paper no. 3, Colorado State University.

Dalla, E., M. Hilpert, and C. T. Miller (2002), Computation of the interfacial area for two-fluid porous medium systems, *J. Cont. Hydr.*, *56*, 25–48.

Dillard, L. A., H. I. Essaid, and M. J. Blunt (2001), A functional relation for field-scale non-aqueous phase liquid dissolution developed using a pore network model, *J. Cont. Hydr.*, *48*, 89–119.

Dong, M., F. A. L. Dullien, and I. Chatzis (1995), Imbibition of oil in film form over water present in edges of capillaries with an angular cross section, *J. Coll. Int. Sci.*, *172*, 21–36.

Faisal Anwar, A. H. M., M. Bettahar, and U. Matsubayashi (2000), A method for determining air–water interfacial area in variably saturated porous media, *J. Cont. Hydr.*, *43*, 129–146.

Gladkikh, M., and S. Bryant (2003), Prediction of interfacial areas during imbibition in simple porous media, *Adv. Water Resources*, *26*, 609–622.

Gray, W. G. (1999), Thermodynamics and constitutive theory for multiphase porous-media flow considering internal geometric constraints, *Adv. Water Resources*, *22*(5), 521–547.

Hassanizadeh, S. M., and W. G. Gray (1993), Thermodynamic basis of capillary pressure in porous media, *Water Resources Research*, *29*(10), 3389–3405.

Held, R., and M. A. Celia (2001), Modeling support of functional relationships between capillary pressure, saturation, interfacial area and common lines, *Adv. Water Resources*, *24*, 325–343.

Helland, J. O., and S. M. Skjæveland (2004), Physically-based capillary pressure correlation for mixed-wet reservoirs from a bundle-of-tubes model, paper SPE 89428 presented at the SPE/DOE Fourteenth Symposium on Improved Oil Recovery, Tulsa, OK, Apr. 17–21. Revision accepted for publication in SPE Journal.

Hui, M., and M. J. Blunt (2000), Effects of wettability on three-phase flow in porous media, *J. Phys. Chem. B*, *104*, 3833–3845.

Kennedy, C. A., and W. C. Lennox (1997), A pore-scale investigation of mass transport from dissolved DNAPL droplets, *J. Cont. Hydr.*, *24*, 221–246.

Kovscek, A. R., H. Wong, and C. J. Radke (1993), A pore-level scenario for the development of mixed wettability in oil reservoirs, *Am. Inst. Chem. Eng. J.*, *39*(6), 1072–1085.

Ma, S., G. Mason, and N. R. Morrow (1996), Effect of contact angle on drainage and imbibition in regular polygonal tubes, *Coll. and Surf. A: Phys. and Eng. Asp.*, *117*, 273–291.

Oostrom, M., M. D. White, and M. L. Brusseau (2001), Theoretical estimation of free and entrapped nonwetting–wetting fluid interfacial areas in porous media, *Adv. Water Resources*, *24*, 887–898.

Or, D., and M. Tuller (1999), Liquid retention and interfacial area in variably saturated porous media: upscaling from single-pore to sample-scale model, *Water Resources Research*, *35*(12), 3591–3605.

Øren, P., S. Bakke, and O. Arntzen (1998), Extending predictive capabilities to network models, *SPE Journal*, pp. 324–336.

Reeves, P. C., and M. A. Celia (1996), A functional relationship between capillary pressure, saturation and interfacial area as revealed by a pore-scale network model, *Water Resources Research*, *32*(8), 2345–2358.

Saripalli, K. P., P. S. C. Rao, and M. D. Annable (1998), Determination of specific NAPL–water interfacial areas of residual NAPLs in porous media using the interfacial tracers technique, *J. Cont. Hydr.*, *30*, 375–391.

Schaefer, C. E., D. A. DiCarlo, and M. J. Blunt (2000a), Experimental measurement of air-water interfacial area during gravity drainage and secondary imbibition in porous media, *Water Resources Research*, *36*(4), 885–890.

Schaefer, C. E., D. A. DiCarlo, and M. J. Blunt (2000b), Determination of water-oil interfacial area during 3-phase gravity drainage in porous media, *J. Coll. Int. Sci.*, *221*, 308–312.

Schäfer, A., P. Ustohal, H. Harms, F. Stauffer, T. Dracos, and A. J. B. Zehnder (1998), Transport of bacteria in unsaturated porous media, *J. Cont. Hydr.*, *33*, 149–169.

van Dijke, M. I. J., and K. S. Sorbie (2006), Existence of fluid layers in the corners of a capillary with non-uniform wettability, *J. Coll. Int. Sci.*, *293*, 455–463.

van Genuchten, M. T. (1980), A closed-form equation for predicting the hydraulic conductivity of unsaturated soils, *Soil Sci. Soc. Am. J.*, *44*, 892–898.